10th International Conference on Fracture Mechanics of Concrete and Concrete Structures
FraMCoS-X
G. Pijaudier-Cabot, P. Grassl and C. La Borderie (Eds)
https://doi.org/10.21012/FC10.235475

Fracture Mechanism of Reinforced Concrete Non-Structural Wall

MIKI MATSUBAYASHI[*], MASAMICHI TAKAHASHI[†], RYOHEI KUBOTA[†],

YUYA TAKASE[†] AND MITSUO MIZOGUCHI[†]

[*] Muroran Institute of Technology
Hokkaido, Japan
e-mail: 18041070@mmm.muroran-it.ac.jp

[†] Muroran Institute of Technology
Hokkaido, Japan
e-mail: 18041045@mmm.muroran-it.ac.jp, 18041027@mmm.muroran-it.ac.jp, y.takase@mmm.muroran-it.ac.jp, mitsuo@mmm.muroran-it.ac.jp

Key words: Non-structural wall, Shear crack, Full size experiment, FE analysis

Abstract: Following recent earthquakes in Japan, there are several reports of damage to non-structural walls in reinforced concrete buildings, which causes problems for their continued use. Thus, it is important to consider structural strength as well as damages in design. In this paper, we propose a performance design method to evaluate the fracture mechanism of non-structural walls. In other words, we propose a method to evaluate the levels of shear crack (i.e., width, number of cracks, and crack width) to determine the relationship between shear load and deformation. We focus specifically on crack width. First, we conducted an experiment on the walls and investigated the influence of the rebar arrangement on cracks. The shear strength increases, and the crack width was found to decrease when the rebar separation became narrower and the rebar ratio increased. Subsequently, we reproduced the behaviors of the test specimens observed in the earlier experiments via FEA. Further, we propose a method to calculate the crack width. We also propose a formula for the maximum strain of rebar necessary to calculate the crack width.

1 INTRODUCTION

Japan is a heavily earthquake-prone country, and several buildings are damaged by earthquakes. However, the risk of large-scale disasters including building collapse decreased recently with the development of seismic-resistant designs. Nevertheless, the effects of tsunamis [1, 2] and damage to piles due to liquefaction [3] are observed following the 2011 Tōhoku earthquake off the Pacific coast. Additionally, damage to non-structural walls was also reported [4, 5] after the Tōhoku earthquake and the 2016 Kumamoto earthquake.

Non-structural walls, such as spandrel walls, hanging walls and mullion walls, are architectural elements that do not require structural design. Thus, they are not expected to exhibit significant structural and aseismic capacity, and they will not affect structural safety even if these elements are damaged or in failure. Thus, as previously mentioned, there are several reports of significant damage to non-structural walls after the occurrence of

Figure 1:An example of a damaged non-structural wall in the 2016 Kumamoto earthquake

major earthquakes in recent years. **Figure 1** shows an example of a damaged non-structural wall after the 2016 Kumamoto earthquake.

Although damaged non-structural walls do not affect structural safety, they can cause other problems. For example, it is necessary to demolish the building in certain cases where fast recovery is impossible due to decreased usability or high repair costs. Therefore, it is vital to address the problems of non-structural damage, such as non-structural walls, for the continued use of a building after an earthquake. There are a few methods to solve the problems. Inoue *et al*. developed non-structural walls with ductile properties and examined the manner in which they absorb earthquake energy [6].

It is also important to develop a method that estimates the amount of damage to a structure. If the amount of damage can be estimated reasonably and is known before a strong earthquake, then it is easier to prepare for repairs or the burden of repair costs. An indicator of the amount of damage sustained corresponds to the crack width. In the study, we propose a formula to calculate the crack width. The maximum strain value of the rebar is necessary for the formula. We propose a method to calculate that value.

1.1 Purpose of the study

In extant studies [7, 8], a method was proposed to calculate the maximum shear crack width, and the validity of the method was verified by comparing the experimental values with the calculated values. We conducted loading experiments. We used a total of four full size wall specimens. The specimens were assumed as RC non-structural walls. We used the rebar spacing and rebar ratio as parameters and investigated the effect of the rebar arrangement on the occurrence of cracks. Furthermore, we reproduced the behaviors of the RC non-structural walls observed in the experiment via FEA. Additionally, we proposed a crack width calculation method and compared it with experimental results to verify the validity of the proposed method.

2 TEST PLAN AND TEST RESULTS

2.1 Details of specimens

Four specimens were manufactured. The specimens assumed a roughly square, non-structural wall, adjacent to the opening. **Table 1** shows the parameters of each specimen. **Table 2** shows the results of material tests of the concrete, and **Table 3** shows the results of material tests of the rebar.

Specimens exhibited a wall cross section of 100 mm × 750 mm and a wall height of 750 mm. We used ready-mixed concrete. The axial load ratio was 0.15. **Figure 2** shows the shapes and rebar arrangement of S110. The shape and rebar arrangement of the loading beam and

Table 1: Parameter of specimens

Specimens	S110	S220	S280	M200
Wall thickness (mm)	100			
Wall length (mm)	750			
Wall height (mm)	750			
Rebar spacing (mm)	110	220	280	200
Rebar ratio (%)	0.29	0.29	0.26	0.52
F_c(N/mm^2)	18			
Axial load (kN)	308	303	291	300
	Axial load ratio: 0.15			

Table 2: Material test data of concrete

Specimens	f_c(N/mm^2)	E_c(kN/mm^2)	f_t(N/mm^2)
S110	27.5	22.2	2.15
S220	27.0	22.0	2.17
S280	25.9	21.9	2.01
M200	26.8	21.9	1.96

f_c: Compressive strength, E_c: Young`s modulus, f_t: Split strength

Table 3: Material test data of rabar

Part	ϕ	f_y (N/mm^2)	f_u (N/mm^2)	E_s (kN/mm^2)	ε_y (%)
Wall rebar	D6	439	571	184	0.25
	D10	400	549	172	0.24
Opening rebar	D16	387	580	175	0.24

f_y: Yield strength, f_u: Tensile strength, E_S: Young`s modulus, ε_y: Strain

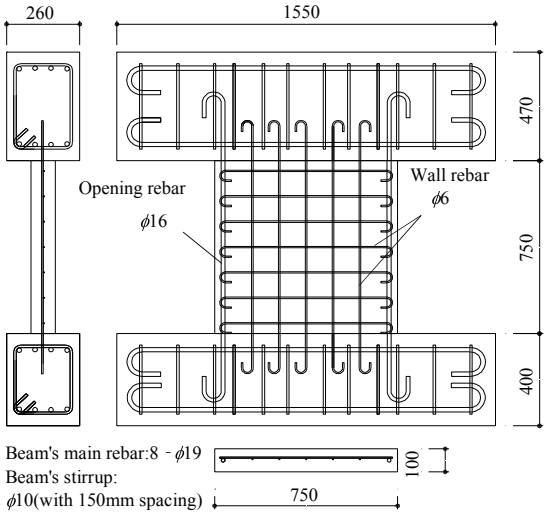

Figure 2: Specimen diagram of S110

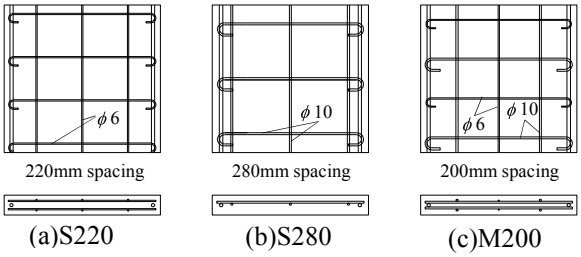

Figure 3: Specimen diagram of S220, S280 and M200

bottom beam are common across the specimens. **Figure 3** shows the rebar arrangement of the other three walls. In several previous experiments, the rebar ratio was simultaneously changed while using the rebar spacing as a parameter. However, in the experiment, the influence of rebar spacing and rebar ratio on each specimen was investigated.

Thus, the rebar arrangement was designed such that only either of the rebar spacing and the rebar ratio fluctuated. Additionally, S220 was used as a reference rebar arrangement. The rebar arrangements of S220 corresponded to ϕ6 (with a spacing of 220 mm) for the wall rebar in both vertical and horizontal directions and ϕ16 for the opening reinforcement bar. The wall rebar corresponded to a double arrangement. In all specimens, opening reinforcement bars were common. The rebar ratio of S220 was 0.29%. The rebar ratio of S110 and S280 were almost identical to that of S220. The rebar arrangements of S110 corresponded to ϕ6 (with a spacing of 110 mm) for the wall. The rebar arrangements of S280 corresponded to ϕ10 (with a spacing of 280 mm) for the wall.

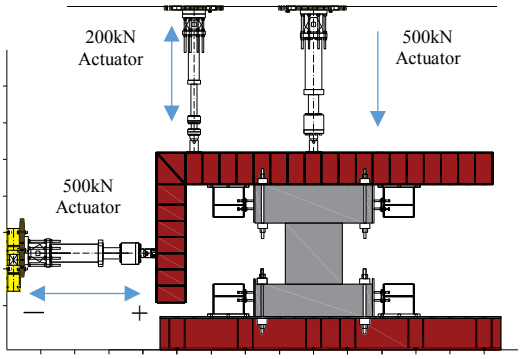

Figure 4: Loading setup

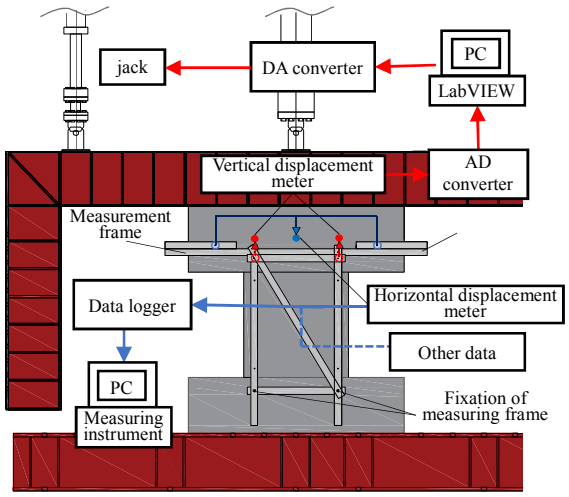

Figure 5: Flow of data measurement

Furthermore, M200 exhibited almost the same rebar spacing as S220 although the rebar ratio was different. The rebar arrangements of M200 corresponded to ϕ6, 10 (with a spacing of 200 mm) for the wall. The wall rebar corresponded to a double arrangement and M200 exhibited a rebar ratio of 0.56%. The size of the loading beam and the bottom beam corresponded to 1550 mm×260 mm×470 mm and 1550 mm×260 mm×400 mm, respectively. We used 8-ϕ19 for the main rebar and ϕ10 (with 150-mm spacing) for the hoop rebar.

2.2 Loading method

In each specimen, the horizontal loading was obtained via reversed cyclic shear loading after applying a constant axial load. We controlled the horizontal load according to the drift angle R, which was calculated according to dividing the horizontal displacement of the loading beam by the wall height.

Figure 4 shows the loading setup. The horizontal load was applied such that the loading beam was parallel to create an antisymmetric moment. In order to maintain the parallel state, two actuators were used in the vertical direction. An actuator applied axial load at the center position of the wall. Another actuator was controlled such that the loading beam and bottom beam were parallel. **Figure 5** shows the flow of automatic control and data measurement method. The procedure is as follows. (1) We measured the vertical displacement of the two points of the beam in order to confirm whether the two beams are parallel. (2) An AD converter was used to convert the measured value into a digital signal. (3) We used a control program software (LabVIEW) to calculate the output voltage such that it became parallel. (4) We converted the output voltage into an analog signal to control the actuator.

In the horizontal direction, positive and negative alternating repetitive incremental loads were applied by the actuator installed at the center height position of the wall .The horizontal load was gradually increased, and the horizontal loading steps were as follows: $R = 0.1\times10^{-2}$, 0.2×10^{-2}, 0.3×10^{-2}, 0.4×10^{-2}, 0.5×10^{-2}, and 0.6×10^{-2} radian. The loads were applied once each.

2.3 Measurement method of rebar strain and crack width

Rebar strains were measured with a strain gauge attached to wall rebar and opening rebar. The strain gauges were evenly pasted to the lateral rebars of the wall. For the vertical streak of the wall, we pasted a strain gauges only near the diagonal of the wall. Crack scale was used for crack width measurement. Perform measurement at peak deformation of each cycle and at unloading (0 kN). Cracks and pellings that could be visually confirmed were recorded by sketching. The crack width is measured on both surfaces of the wall. We only sketched the beam and wall side.

2.4 Experimental results

2.4.1 Features of maximum load and load deformation relationship

Table 4 shows the maximum load Q_{max}, the deformation angle at the maximum load R_{max}, critical deformation angle R_u (considered as the point reduced to 80% of the maximum load), and calculated maximum load. The bending strength calculation value Q_{mu} corresponds to a value that considers only the opening reinforcement bar as the tensile rebar. Additionally, the shear strength calculated value Q_{su} corresponds to the non-structural wall based on the reference [9]. For example, it is calculated by multiplying the wall length of 750 mm by 0.95 as the effective length of the wall. Equation (1) and Equation (2) denote the calculation formulae. The meaning of each symbol is shown in appendix 1).

$$Q_{mu} = 2\left\{0.8\sigma_t a_t l + 0.5Nl\left(1-\frac{\mathrm{N}}{tlF_c}\right)\right\}/h \quad (1)$$

$$Q_{su} = \gamma\left\{\frac{0.068{p_{te}}^{0.23}(18+F_c)}{\sqrt{\frac{M}{Ql}+0.12}} + 0.85\sqrt{p_{se}\sigma_{wy}} + 0.1\sigma_0\right\}t_e j_e \quad (2)$$

In **Table 4**, S110, S220, and S280 with similar rebar ratios and different rebar spacing are compared. The maximum load decreased when rebar spacing increased. We compared S220 and M200. It was confirmed that the maximum load decreased when the rebar ratio decreases. In the specimen S220, the load gradually decreased after the maximum load, and it was possible to measure the critical deformation angle. However, it was observed that the other specimens failed before the load decreased to 80% of the maximum load and that they were broken in a fragile manner.

Figure 6 shows the load deformation curve of each specimen. It indicates the points of maximum load and points where wall rebar and opening reinforcement bar yield. In S110 with minimum rebar spacing, the maximum load

Table 4: Maximum load, maximum deformation angle

		S110	S220	S280	M200
Q_{max} (kN)	+	305	272	260	301
	-	-268	-251	-249	-282
R_{max} ($\times 10^{-2}$rad.)	+	0.23	0.20	0.21	0.40
	-	0.39	0.23	0.27	0.41
R_u ($\times 10^{-2}$rad.)		—	0.71	—	—
Q_{mu}(kN)		385	380	372	380
Q_{su}(kN)		322	311	315	338

*Only the S220 was able to measure up to the load reduced to 80% of the maximum load

corresponded to 305kN when $R = 0.23 \times 10^{-2}$ rad. Following this, the crack expanded and shear fracture occurred in the cycle of $R = 0.50 \times 10^{-2}$ rad. In S110, the highest maximum load among the four specimens was observed. When compared with the standard specimen S220, the maximum load was 12% higher. Furthermore, S220 exhibited a maximum load of 272kN when $R = 0.20 \times 10^{-2}$ rad. Additionally, S220 exhibited failure in the cycle corresponding to $R = 0.60 \times 10^{-2}$ rad.. Simultaneously, compression struts were generated among the diagonal line of the wall, and compressive failure of the wall corners was also confirmed. Moreover, S280 exhibited a maximum load of 260kN when $R = 0.21 \times 10^{-2}$ rad. Additionally, S280 failed in the cycle of $R = 0.40 \times 10^{-2}$ rad. It corresponded to the specimen with the lowest maximum load among the four specimens. Furthermore, M200 (which exhibits almost the same rebar spacing as S220) exhibited the maximum load corresponding to 301kN when $R = 0.40 \times 10^{-2}$ rad. Thereafter, at $R = 0.50 \times 10^{-2}$ rad. cycle, shear failure occurred due to increases in the crack width caused by slant tension. The deformation angle of this specimen at the maximum load corresponded to the highest among all specimens. While observing the failed behavior during the experiment, shear cracks occurred at the initial stage of loading with a large noise on all the test specimens. Cracks generated at the initial stage of loading expanded and caused severe damage.

2.4.2 Crack occurrence

Figure 7 shows the crack patterns at $R = 0.2 \times 10^{-2}$ rad. cycles and 0.4×10^{-2} rad. cycles for each specimen and the photograph of the specimen at the end. Black lines and red lines in the figure denote cracks generated on the positive side and loading at the negative side, respectively. Points are denoted in the crack diagram of the cycle of $R = 0.4 \times 10^{-2}$ rad. The point denotes the measurement point of the maximum crack width. Measurement points at

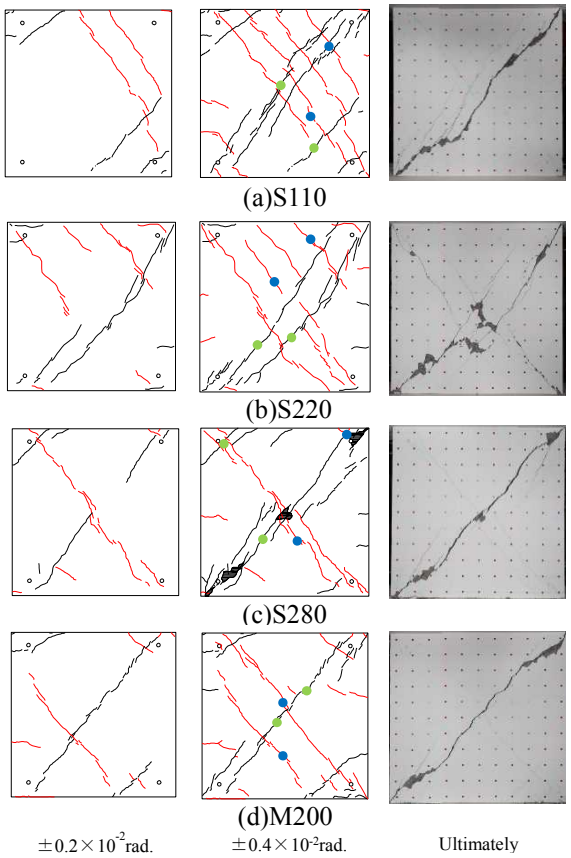

Figure 7: Maximum crack generation diagrams

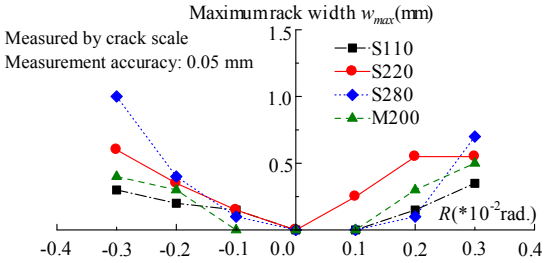

Figure 8: Maximum crack width

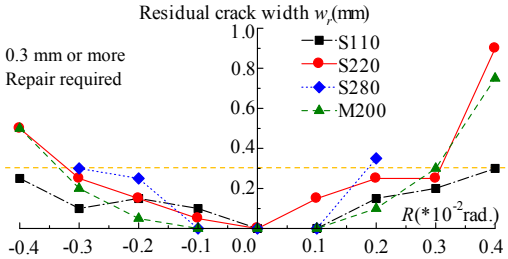

Figure 9: Maximum residual crack width

the time of positive side loading are denoted by green points and measurement points at negative side loading are denoted by blue points. There are multiple green and blue dots given the differences in the measurement positions at the beginning and the end of loading. Shear cracking occurred in all specimens. In S110, diagonal cracks gradually occurred at the corners of the wall. Following this, large diagonal shear cracks occurred at the center of the wall at $R = 0.4 \times 10^{-2}$ rad. cycles. When compared with other specimens, the number of cracks was high, the spacing decreased, and the crack width decreased. At S220, shear cracking occurred diagonally at $R = 0.1 \times 10^{-2}$ rad. cycles. Cracks on the diagonal occurred even in subsequent cycles. Compressive failure eventually occurred near the center of the compressive strut. This, it often corresponded to exfoliation, and there was significant damage even at the corners and the boundary with the beam. In S280, shear cracks on the diagonal occurred at $R = 0.2 \times 10^{-2}$ rad. cycles. It corresponded to a specimen with large rebar spacing. Therefore, the crack width was high and the number of cracks was low. In M200, shear cracks on the diagonal occurred at $R = 0.2 \times 10^{-2}$ rad. cycles.

2.4.3 Measurement result of crack width

Figure 8 shows the maximum crack width transition for each specimen up to $R = 0.3 \times 10^{-2}$ rad. The measurement of the maximum crack width was performed by decreasing the load by approximately 10% after reaching the peak displacement of each cycle. In the vicinity of the maximum load, the crack width increased when the rebar spacing increased on both the positive side and negative side. When $R = -0.3 \times 10^{-2}$ rad., the crack width of S280 was approximately four times that of S110. Furthermore, the crack width decreased when the rebar ratio increased. The behavior of the crack width gradually opened when the rebar spacing decreased and the rebar ratio increased. **Figure 9** shows the transition of the maximum residual crack width. The residual crack width was measured when the load decreased to 0kN with reductions in the peak of each cycle. When

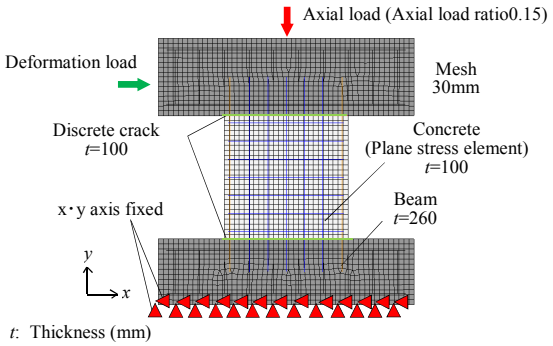

Figure 10: Mesh diagram

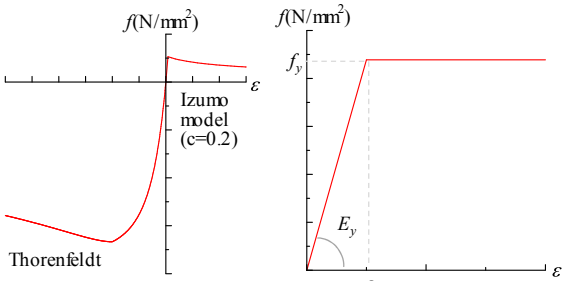

Figure 11: Material constitution law

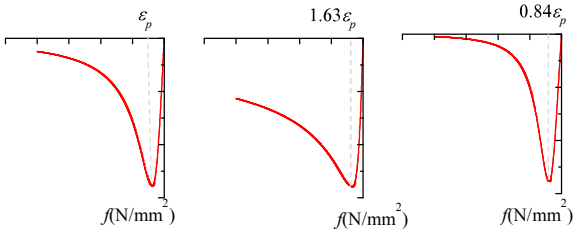

Figure 12: Thorenfeldt changing the value of n

the maximum residual crack width was 0.3 mm or more, a repair was required [10]. As shown in the figure, increases in the rebar spacing increased the residual crack width, and thus a repair was more likely required.

3 FINITE-ELEMENT ANALYSIS

3.1 Outline and goals

In this section, 2D finite-element (FE) analysis is performed. The general-purpose FE program DIANA 10.1 is used [11]. The aim involves estimating the behaviors of the test specimens observed in the earlier experiments as shown in Section 2.

A distributed crack model is typically used for the non-linear FE analysis of reinforced concrete structures as shown in the study.

However, it is not possible to directly use the model to directly estimate accurate crack spacing. Therefore, in the analysis, it is assumed that crack patterns approximately agree with test results and that *Q–R* curves exhibits good agreement with test results until the peak load. Additionally, the purpose of the study is to estimate crack width, and thus it is important to only form estimations up to the angle at which crack widths can still be measured.

3.2 FE mesh

Figure 10 shows the FE mesh. In the figure, specimen S110 is used as an example. The mesh is fully divided into 30-mm-wide squares. The concrete corresponds to a plane stress element, and the rebars correspond to embedded rebar elements. The loading method of the tests used corresponds to an antisymmetric type, and thus the upper loading beam is free in the x direction and restrained such that the y displacements of both edge elements of the loading beam exhibit the same value. In all the FE models, the bottom loading beam is fixed in the x and y directions

3.3 Material properties

The constitutive law of concrete is shown in **Figure 10**. In the analysis, the Izumo model [12,13] is used for the stress versus strain curve of concrete when concrete is subjected to tensile stress. The Izumo model is expressed as follows:

$$\sigma = \begin{cases} E_c\bar{\varepsilon} & \text{for } 0 < \bar{\varepsilon} < \varepsilon_e \\ f_t\left(\dfrac{\varepsilon_{tu}}{\bar{\varepsilon}}\right)^c & \text{for } \bar{\varepsilon} \geq \varepsilon_e \end{cases} \quad (3)$$

where $\bar{\sigma}$ denotes the average stress, $\bar{\varepsilon}$ denotes the average strain, and ε_e denotes the strain at maximum stress. Additionally, ε_{tu} denotes the crack generation strain and c denotes an exponent coefficient for the anchorage of a rebar.

In the stress versus strain curve, Thorenfeldt model is applied on the side subjected to compressive stress. The Thorenfeldt model is described as follows [14]:

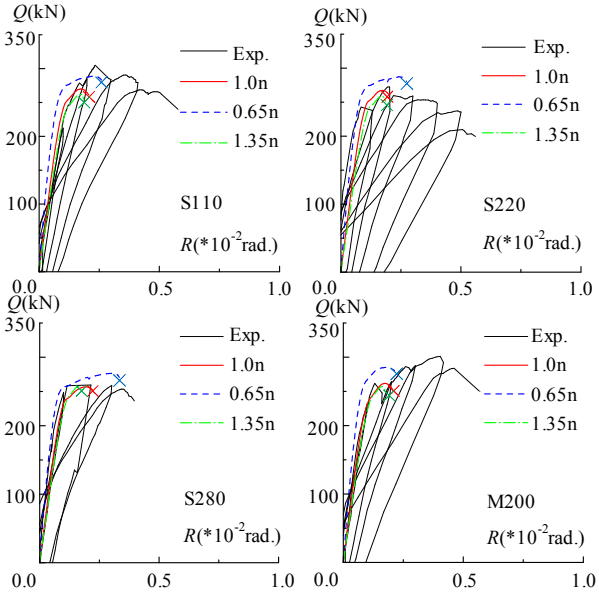

Figure 13: Comparison of load deformation curves

$$f = \left[\frac{n\left(\varepsilon_c/\varepsilon_p\right)}{n-1-\left(\varepsilon_c/\varepsilon_p\right)^{nk}}\right] f_c \quad (4)$$

$$\mathrm{n} = 0.8 + \frac{f_c}{17} \quad (5)$$

$$\mathrm{k} = \begin{cases} 1, & \varepsilon_p < \varepsilon_c < 0 \\ 0.67 + \dfrac{f_c}{62}, & \varepsilon_c \leq \varepsilon_p \end{cases} \quad (6)$$

$$\varepsilon_p = \frac{n}{n-1} \cdot \frac{f_c}{1000E_c} \quad (7)$$

The value of n used in the expression affects the pre-peak and post-peak slope. **Figure 12** shows the structural rule of Thorenfeldt wherein the value of n is changed. We show the constituent rule calculated by the value of n based on extant studies, and the value of n obtained by multiplying it by 0.65 and 1.35. With respect to the pre-peak, decreases in n increase the ε_p. However, the stiffness increases when the value of n decreases. With respect to the post-peak, if n is lower than the reference, then it becomes a gentle curve. If n exceeds the reference, then it changes to a slightly steep curve although the difference is slight. We change n and perform FEA to understand how this affects the analysis.

3.4 Analysis results

Figure 13 shows the relationship between the shear load Q and the member deformation angle R of the experimental values and analysis values. The smaller the value of n, the higher the rigidity as in the constitutive law. Also the maximum load increased. Regarding the increase in the maximum load, when the value of n decreases in the constitutive law, the post-peak tends to be gentle. Therefore, it is presumed to be slowly destroyed. In the analysis in which n is reduced, it is considered that the maximum load increased because damage gradually occurred. In any condition, shear fracture could be confirmed regardless of the curve at post-peak. The destroyed points are indicated by " x ". Looking at the destroyed point, 3 specimens other than M200 are generated where the value of n is small, the point has a deformation angle larger than that of other analysis. However, for M200, it can be seen that it is destroyed at the same deformation angle as other analysis conditions. It can be expected that the large reinforcing bar ratio has some influence. In reproducing the load deformation curve, it can be seen that there are some specimens suitable for 0.65 n and specimens suitable for n and 1.35 n. Therefore, it is considered that there is no problem to correct the value of n depending on the conditions of the specimen. **Figure 14** shows the distribution of the maximum principal strain E_1 of S220. The status of $R = 0.6\times10^{-3}$, 1.3×10^{-3}, 2.0×10^{-3} rad. are displayed, respectively. $R = 2.0 \times 10^{-3}$rad. is just before shear failure occurs in analysis. Distortion concentrates on the diagonal of the wall as the deformation progresses. **Figure 15** shows the strain distribution of the horizontal and vertical rebars. It shows the same deformation angle as in **Figure 14**. Basically, the distortion in the central part of the wall is large. In the experiment large shear failure occurred on the diagonal of the wall. From **Figures 14** and **15**, we can understand that it is reproduced by analysis. Also, in the experiment, cracks occurred in the corners of the wall at the initial stage of loading. **Figure 14** also reproduces it.

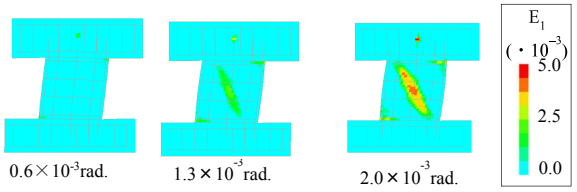

Figure 14:Maximum principal strain distribution

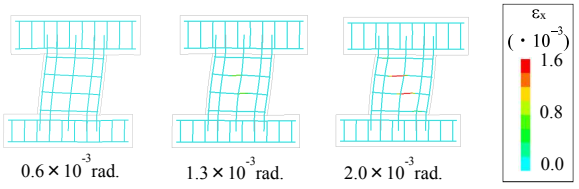

(a)Horizontal rebar

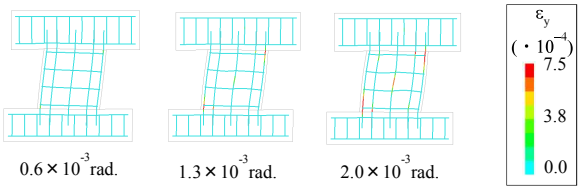

(b)Vertical rebar

Figure 15: Strain Distribution of Rebar

4 PROPOSAL OF CRACK WIDTH CALCULATION FORMULA

Silva *et al*. proposed a formula to estimate the average shear crack width of an I-shaped pre-stressed reinforced concrete beam [15]. Based on the formula, the study proposes a method to estimate the maximum shear crack width for a non-structural wall.

The maximum crack width w_{max} and average crack interval s_{av}, are estimated as follows:

$$w_{max} = k_w s_{av} \varepsilon_{max} \sin\theta \qquad (8)$$

$$s_{av} = 2\left[c + \frac{2s}{10}\right] + k_1 k_2 \frac{\phi}{\rho_r} \qquad (9)$$

If horizontal rebar and vertical rebar are arranged in vertical, k_w is set to 1.2. Additionally, ε_{max} denotes the maximum strain of the rebar at each deformation angle, c denotes the concrete cover, s denotes the spacing of rebar, k_1 for deformed bars is 0.4, and k_2 is 0.25 when $s \leqq 15\phi$ and 0.1 when $s > 15\phi$. Only the condition for $s \leqq 15\phi$ was described in extant studies. Non-structural walls are characterized via large rebar spacing,

Table 5: Additional specimen parameters

Specimens	*M/Qd*	Rebar specing *s*(mm)	Rebar ratio p_{wh} (%)
S250	0.95	250	0.25
L60		60	0.99
S175	0.67	175	0.32
L50		50	1.19

and thus conditions were added to calculate non-structural walls. Furthermore, ρ_r denotes rebar ratio. In the previous study, the maximum strain of the rebar as obtained by FEA is applied in the calculation. However, it is difficult to perform FEA every time to calculate the crack width. Therefore, in the study, we propose a simple method to calculate the maximum rebar strain. Equation (3) provides the formula for the maximum rebar strain ε_{max} where h denotes the wall height, d denotes the width of the wall, and x denotes the horizontal displacement.

$$\varepsilon_{max} = \left(h - \sqrt{x^2 + (x \cdot \frac{h}{d})^2} \right) \Big/ h \qquad (10)$$

Figure 16 shows an image diagram to geometrically calculate the strain of the reinforcing bars. The dotted line shows the strain before loading and the solid line shows the strain after loading. Equation (3) is derived based on this. It is assumed that the strain of the rebar is identical to the strain of the concrete. Based on the horizontal and vertical displacement, Pythagorean theory is applied to calculate the deformed wall length. Subsequently, the displacement amount of the wall is calculated. Finally, the maximum rebar strains are calculated by dividing the displacement of the wall by the original length of the wall. We consider the validity of the crack width calculation formula shown above. In the study, the previous test results are used for validation. The number of the additional specimens is four [16, 17], and thus the total specimen number is eight. The crack width transition in a total of eight specimens is compared with the experimental values and calculated values. **Table 5** shows parameters of

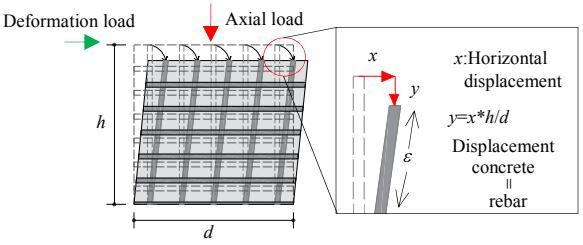

Figure 16: Strain image

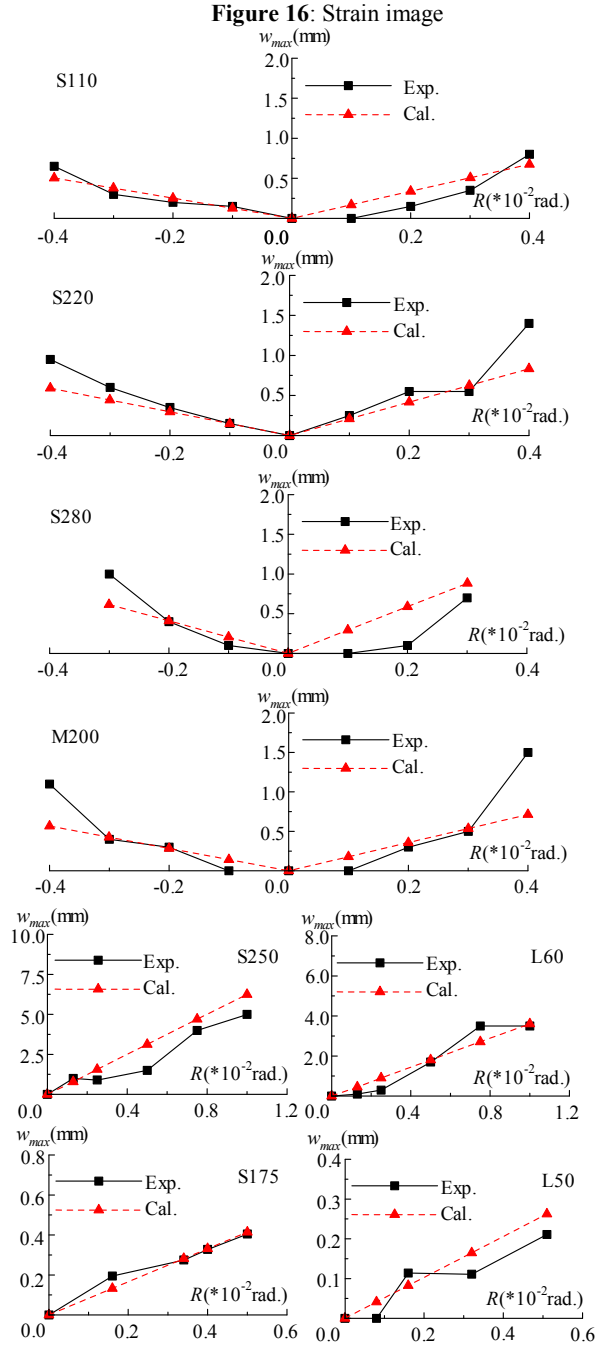

Figure 17: Comparisons of crack width

the additional specimens. **Figure 17** shows a comparison between the experimental value and calculated crack width. Several specimens exhibit well matched experiment values and

calculated values. A few specimens with calculated values below the experimental values are also observed. Specimens in which the calculated value significantly exceeded the experimental value are not observed, and thus the formula potentially underestimates crack width.

5 CONONCLUSION

In this study, we focused on the crack width and conducted experiments and analyses to examine the damage mechanism of the non-structured wall. The obtained findings are as follows:

1) The crack width increases when the rebar spacing is wider or the rebar ratio decreases.
2) We attempted to reproduce the failure mode by 2D-FEA. We investigated the effect of the load deformation curve via the value of *n* constituting Thorenfeldt model that corresponds to the material constitution law.
3) We proposed a maximum shear crack width calculation method and a simple formula to calculate the maximum strain of rebars. The crack width was reasonably estimated via the proposed method.

A future study will involve more specimens and data to reproduce load deformation curve and crack width transitions.

References

[1] Carden L. P. and Chock G. Y. K.: Structural mitigation of building damaged by the 2011 Tohoku Tsunami using the ASCE 7 Tsunami design provisions. 16th World Conference on Earthquake, 16WCEE 2017; Paper No.1029.

[2] Norton T. R. and Murao O.: Debris management and restoration of the Miyagi prefecture after the 2011 Tohoku earthquake and Tsunami. 16th World Conference on Earthquake, 16WCEE 2017; Paper No.4166.

[3] Tokimatsu K., Suzuki H. and Abe A.: Performance of three different pile foundations in Urayasu city curing 2011 Tohoku Earthquake. 16th World Conference on Earthquake, 16WCEE 2017; Paper No.2735.

[4] Nakamura A. Teshigawara M. and Hirabayashi T.: Failure mechanism of beam-column joint of reinforced concrete frame with non-structural walls. 16th World Conference on Earthquake, 16WCEE 2017; Paper No.2746.

[5] Yoon R. H., Sanada Y. and Akahori T.: Analytical simulations on structural experiments of one-story one-bay R/C moment-resisiting frames with non-structural walls. 16th World Conference on Earthquake, 16WCEE 2017; Paper No.423.

[6] Inoue K., Iso, Y., Takase, T., Saito and K., Ishikawa K.: Structural characteristics of concrete walls for absorbing earthquake energy. Journal of advanced civil engineering practice and research, 2017; 5:17-23.

[7] Matsubayashi, M., Takase,Y., Mizoguchi,M. and Inoue,K.: Estimation of crack width of non-structural walls using finite-element analysis, Journal of Advanced Civil Engineering Practice and Research, Vol.6, pp.18~25 Jun.2018

[8] Matsubayashi,M.,Takase,Y.,Mizoguchi,M. : Proposal and Verification of Crack Width Estimation Method of Non-Structural Wall Using FEM Analysis, Summaries of technical papers of annual meeting Architectural Institute of Japan, pp.457-458, 2018.9 (in Japanese)

[9] Architectural Institute of Japan : AlJ Standard for Structural Calculation of Reinforced Concrete Structures, p.292, 2010.2. (in Japanese)

[10] Mukai T. : Research results on seismic design method utilizing the lessons learned in the Great East Japan Earthquake-Construction of seismic performance design and evaluation method for ensuring continued usability after earthquake of government buildings, evacuation facilities, etc.-, BRI-H27 Lecture text, 2015.3. (in Japanese)

[11] DIANA 10.1 User's manual: https: //dianafea.com/manuals/d101/Diana.html

[12] Tamai S., Shima H., Izumo J. and Okamura H.: Average stress-average strain

relationship of steel in uniaxial tension member in post-yield range, JSCE Vol.378, V-6, 1987.2. (in Japanese)

[13] Sato Y., Tadokoro T. and Ueda T.: Diagonal Tensile Failure Mechanism of Reinforced Beams. Journal of Advanced Concrete Technology, Vol.2, No3, 327-341, 2004.10.

[14] Maki Y., Minh H.T., Fukuda S., Torii K. and Ono R.: Stiffness Evaluation and Current Status of a Degraded Road Bridge Slab Located in a Mountainous Area, Journal of Advance Concrete Technology, Vol.17, 62-78, 2019.1.

[15] Silva D. S., Mutsuyoshi H. and Witchukreangkrai E.: Evaluation of Shear Crack Width in I-Shaped Reinforced Concrete Beams, Journal of Advanced Concrete Technology, Vol.6, No3, 443-458, 2008.8.

[16] Tani M., Yuniarsyah E., Mukai T. and Kawano S.: Experimental test for damege redusing and improvement of structural performance of R/C non-structural walls, Proc. of JCI, Vol.37, No2, 2015.6. (in Japanese)

[17] Tani M., Ogura M., Mukai Y. and Taleb R.: Experimental study on failure mode and damage of R/C non-structural walls using actual-scale specimen, Proc. of JCI, Vol.36, No2, 2014.6. (in Japanese)

Appendix

1) σ_t: Tensile rebar yield strength (N/mm^2), a_t : Cross sectional area of tensile rebar (mm^2), l: Wall length (mm), N : Axial load(kN), t: Wall thickness (mm), F_c : Concrete design strength (N/mm^2), h : Wall height(mm), γ: Reduction rate by opening, p_{te}:Tensile rebar ratio, M/Ql:Shear span ratio, p_{se}: Horizontal rebar ratio, w_y: Equivalent horizontal rebar standard yield point (N/mm^2), σ_0:Axial stress(N/mm^2), t_e: Equivalent wall thickness (mm), j_e: Stress center distance (mm)